Journal of the Neurological Sciences 468 (2025) 123358

Contents lists available at ScienceDirect

Journal of the Neurological Sciences

journal homepage: www.elsevier.com/locate/jns

MRI-based morphometric structural changes correlate with histopathology in experimental autoimmune encephalomyelitis

Anna Lowinski [a], Andreas Dabringhaus [b], Matthias Kraemer [b,d], Hardik Doshi [c], Alicia Weier [a], Maik Hintze [a,1], Rittika Chunder [a,1], Stefanie Kuerten [a,*]

[a] Institute of Neuroanatomy, Faculty of Medicine, University of Bonn and University Hospital Bonn, Nussallee 10, 53115 Bonn, Germany
[b] VGMorph GmbH, Waterloostr. 32, 45472 Mülheim an der Ruhr, Germany
[c] Deutsches Zentrum für Neurodegenerative Erkrankungen (DZNE), Venusberg-Campus 1, 53127 Bonn, Germany
[d] NeuroCentrum, Am Ziegelkamp 1f, 41515 Grevenbroich, Germany

ARTICLE INFO

Keywords:
Experimental autoimmune encephalomyelitis
Magnetic resonance imaging
Multiple sclerosis
T1
T2
T2*
Voxel-guided morphometry

ABSTRACT

Background and objectives: Magnetic resonance imaging (MRI) and neurohistopathology are important correlates for evaluation of disease progression in multiple sclerosis (MS). Here we used experimental autoimmune encephalomyelitis (EAE) as an animal model of MS to determine the correlation between clinical EAE severity, MRI and histopathological parameters.

Methods: $N = 11$ female C57BL/6J mice were immunized with human myelin oligodendrocyte glycoprotein 1–125, while $N = 9$ remained non-immunized. Mice were scanned longitudinally over a period of 13 weeks using a 11.7 Tesla (T) Bruker BioSpec® preclinical MRI instrument, and regional volume changes of the lumbar spinal cord were analyzed using Voxel-Guided Morphometry (VGM). Following the final *in vivo* T1-weighted MRI scan, the lumbar spinal cord of each mouse was subjected to an *ex vivo* MRI scan using T1-, T2*- and diffusion tensor imaging (DTI)-weighted sequences. Tissue sections were then stained for immune cell infiltration, demyelination, astrogliosis, and axonal damage using hematoxylin-eosin staining and immunohistochemistry.

Results: While *in vivo* MRI VGM detected an overall increase in volume over time, no differences were observed between EAE animals and controls. *Ex vivo* MRI showed a generalized atrophy of the spinal cord, which was pronounced in the anterolateral tract. The most striking correlation was observed between EAE score, white matter atrophy in *ex vivo* T1-weighted scans and histological parameters.

Discussion: The data demonstrate that *ex vivo* MRI is a valuable tool to assess white matter atrophy in EAE, which was shown to be directly linked to the severity of EAE and spinal cord histopathology.

1. Introduction

Multiple sclerosis (MS) is a chronic neuroinflammatory demyelinating disease of the central nervous system (CNS) and the most frequent cause of irreversible neurological disability and premature retirement in young adults [1]. The clinical presentation of the disease is heterogenous with patients developing a multitude of symptoms in an unpredictable fashion [2]. The most common course of the disease, *i.e.*, relapsing-remitting MS (RRMS), is characterized by acute episodes of neurological dysfunction (relapses) followed by phases of partial or complete recovery (remission) [3]. After about 10–20 years, most patients with RRMS ultimately develop secondary progressive MS (SPMS) [4], which is characterized by continuous worsening of symptoms over time. About 10–20 % of patients present with primary progressive MS (PPMS), which is defined by a gradual disease progression from the time of onset [5].

The pathological hallmarks of MS are the presence of demyelinating lesions in the white matter of the CNS in addition to gray matter atrophy [6]. The extent of demyelination and axonal loss shows interindividual variability and also differs between lesions of the same patient [6]. Inflammation within and around lesions however is seen in all stages of MS [7] and involves, as suggested by neuropathology and genetic studies, cellular components and secreted factors of both the adaptive and innate immune systems [8], including T cells, B cells and myeloid

* Corresponding author at: Anatomical Institute, Director of the Institute of Neuroanatomy, University Hospital Bonn, Nussallee 10, 53115 Bonn, Germany.
E-mail address: stefanie.kuerten@uni-bonn.de (S. Kuerten).
[1] These authors contributed equally.

https://doi.org/10.1016/j.jns.2024.123358
Received 13 July 2024; Received in revised form 4 December 2024; Accepted 13 December 2024
Available online 17 December 2024

cells.

Overall, the unpredictability of disease development, progression and lesion pathology between patient subgroups and even between individual patients within each MS subgroup makes the diagnosis of the disease difficult, especially at early stages [9]. The diagnosis of MS currently requires the fulfilment of the revised McDonald criteria [10] that combine clinical, laboratory and imaging parameters, the latter being mainly based on magnetic resonance imaging (MRI) [11]. The standardized MRI protocol for the initial assessment of MS combines sagittal T1- and T2-weighted sequences before and after the use of gadolinium-based contrast agents [12]. MRI-based lesion dissemination in space (DIS) and time (DIT) then justifies the diagnosis of MS [13].

MRI imaging is a powerful non-invasive method to detect properties of CNS tissue. As such, several MRI protocols are in use to monitor tissue changes that accompany the development of demyelinating lesions during the course of MS. On the one hand, three-dimensional T1-weighted brain scans of patients provide sufficient anatomical detail to robustly detect lesion dynamics [14]. Use of voxel-guided morphometry (VGM), a software that specializes in automated computing of displacement and volume changes in MRI scans, allows for the evaluation of lesion and atrophy progression over time [15].

On the other hand, diffusion tensor imaging (DTI) is suitable for quantifying demyelination and axonal loss in MS, showing a decrease in fractional anisotropy (FA-values) in inflammatory lesions [16]. T2*-weighted sequences are used for quantifying iron deposition [17], and recent studies have highlighted the clinically relevant association between abnormal brain iron accumulation and clinical dysfunction in MS patients [18]. Indeed, the accumulation of iron indicates the presence of paramagnetic rim lesions (PRL), which are associated with a greater risk of relapse activity as well as disease progression independent of relapse activity (PIRA) [19,20].

Nevertheless, despite the advances in medical imaging as a non-invasive tool to reflect pathological changes in patients with MS [13], inconsistent MRI acquisition protocols between different clinical centers [21] and different levels of experience of the consulting (neuro)radiologist may lead to misdiagnosis of the disease [22] or hamper the correct interpretation of progressive MS [23]. Integrating histopathological parameters with neuroimaging data would help to overcome the limitations of relying only on MRI. However, lesion biopsies from patients with MS are rarely acquired [24]. Furthermore, the available tissue samples underlie a bias since most are from older patients and hence predominantly include chronic lesions [25] or only represent a small part of a lesion [24]. Hence, the use of animal models can be useful not only to expand our understanding of the pathology and evolution of CNS lesions but also to study their association with MRI parameters. The direct comparison of MRI with tissue pathology can help to validate the accuracy of the imaging technique [26] and to draw conclusions about the underlying tissue pathology from non-invasive neuroradiological imaging, therefore representing a bridge between neuroradiology and -pathology [27].

In this study, on the one hand, we aimed to monitor morphometric changes in T1-weighted *in vivo* MRI scans of immunized mice using VGM. Our focus was on the lumbar spinal cord, because this CNS region is prominently histopathologically affected in the human myelin oligodendrocyte glycoprotein $(hMOG)_{1–125}$ model and mainly responsible for the clinical deficits that are reflected by the EAE score [28]. Moreover, we analyzed differences in T1-, T2*- and diffusion-weighted *ex vivo* MRI scans comparing EAE mice and controls. Finally, we set out to determine correlations between clinical EAE, MRI and histopathological parameters.

2. Materials and methods

2.1. Induction of EAE and standard protocol approvals

$N = 20$ female 8-week-old wild-type (WT) C57BL/6J (B6) mice (Charles River, Sulzfeld, Germany) were kept under specific pathogen-free conditions at the animal facility of the Deutsches Zentrum für Neurodegenerative Erkrankungen (DZNE) in Bonn, with a 12 h light/dark cycle and free access to standard rodent diet (Ssniff rat/mouse maintenance). All experiments were approved by the Landesamt für Natur-, Umwelt-, und Verbraucherschutz Nordrhein-Westfalen (LANUV) under the file number 81–02.04.2022.A122 and performed according to the criteria of the German Animal Welfare Law. They also complied with the 3R principles, the "Principles of Laboratory Animal Care" (NIH publication no. 86–23, revised 1985), and the ARRIVE guidelines for reporting animal research [29].

$N = 11$ mice were immunized at the age of eleven weeks with $hMOG_{1–125}$ (Hooke Laboratories, Lawrence, MA, USA) in complete Freund's adjuvant (CFA containing 0.5 mg/mL $MOG_{1–125}$ and 2–5 mg/mL *Mycobacterium tuberculosis*). A volume of 100 µL was injected in both sides of the flank, resulting in a total dose of 100 µg $MOG_{1–125}$ being injected per mouse. Additionally, 110 ng of pertussis toxin (Hooke Laboratories) diluted in 100 µL sterile phosphate-buffered saline (PBS, Thermo Fisher, Waltham, MA, USA) was applied intraperitoneally on the day of immunization and 24 h later. Clinical signs of EAE were monitored daily and mice were scored using the following scale: 0 – no symptoms; 1 – partial or complete paralysis of the tail; 2 – complete paralysis of the tail and weakness of the hind limbs; 3 – complete paralysis of the tail and hind limbs; 4 – quadriplegia; 5 – moribund. A control group of $N = 9$ mice remained non-immunized.

2.2. In vivo MRI acquisition

MRI acquisition was conducted at the animal facility of the DZNE using the 11.7 Tesla (T) Bruker Biospec (R) Small Animal MRI (Ettlingen, Germany) equipped with a planar receive-only surface loop coil with an inner diameter of 15 mm. For *in vivo* acquisitions, mice were scanned six days prior to immunization in order to obtain a baseline MRI for later comparison. We chose the following time points for MRI scans post immunization following the disease course of $hMOG_{1–125}$-induced EAE [28]: 9 days (preclinical EAE), 14 days (peak of EAE), 23 days (subacute EAE), 30 days (disease plateau) and 87 days (chronic EAE). Control animals were scanned at baseline and 78 days later (Fig. 1A). A 10-day difference between EAE and control animals was tolerated for the last time point, which was due to technical issues with the MRI scanner. Anesthesia was applied using 2 % isoflurane (Iso-vet®, 1000 mg/g, Bad Oldesloe, Germany) for the entire duration of each scan (approximately one hour per scan). The lumbar spinal cord was located externally through palpation of the lumbar lordosis and the fourth lumbar vertebral body was identified using the three-plane MRI localizer on Bruker's Paravision software (ParaVision® 7), counting two levels up from the pelvic bone [30]. For *in vivo* MRI scans, 3D isotropic T1-FLASH scans were acquired with a repetition time (TR) of 50 milliseconds (ms), an echo time (TE) of 2.5 ms and a resolution of 0.13 mm × 0.13 mm × 0.13 mm.

2.3. Perfusion and tissue dissection

Within 24 h after the last *in vivo* MRI scan, mice were transcardially perfused using 4 % paraformaldehyde (PFA, Carl Roth, Karlsruhe, Germany). After dissection of the lumbar spinal cord, tissue samples were post-fixed overnight in 4 % PFA, and rinsed the next day in 0.1 M phosphate buffer (pH 7.4). The spinal cord segments were then embedded in 1 % agarose gel in 10 mL syringes for *ex vivo* MRI scans. Vertebra L4 used for orientation in *in vivo* scans could not be precisely located for *ex vivo* tissue dissection. Hence, a larger section of the lumbar spinal cord was harvested to include the spinal cord segment adjacent to the lumbar vertebra 4. We refer to this spinal cord segment as vL4 for "vertebra L4", but note that this segment lies caudally to the actual lumbar spinal cord segment L4 from which the roots of the L4 spinal nerves originate.

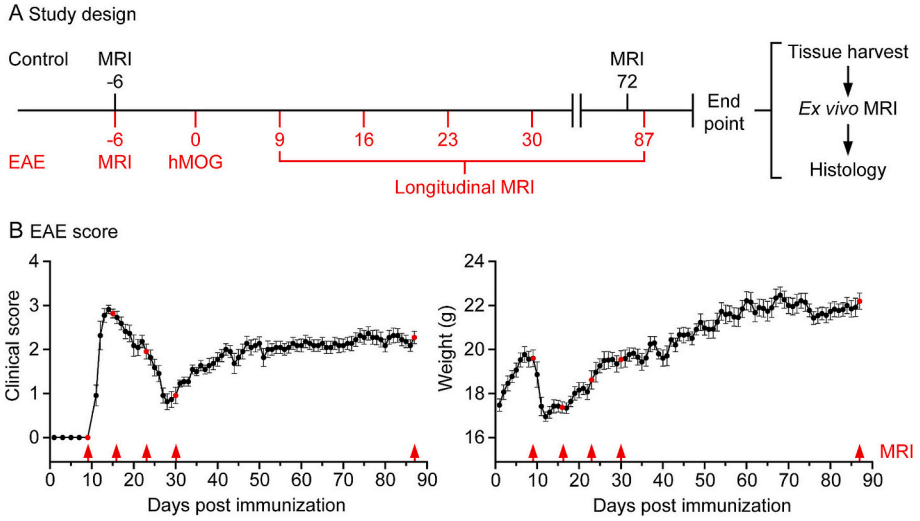

Fig. 1. Study design and EAE induction.
(A) Overview of the experimental setup. For the *in vivo* study protocol, the baseline MRI scan was acquired on average 6 days before immunization of mice with $hMOG_{1–125}$. Immunized animals ($N = 11$) were scanned on days 9, 14, 23, 30 and 87 post-immunization. Controls ($N = 9$) received no immunization and were subjected to only a single endpoint MRI scan 78 days after the baseline scan. After endpoint *in vivo* MRI acquisition, mice were perfusion fixed and the spinal cords were harvested for *ex vivo* MRI scans and histology. (B) Mean clinical EAE scores and weight of immunized animals over the course of the study. Error bars indicate standard errors of the mean. Longitudinal MRI time points are indicated in red. EAE, experimental autoimmune encephalomyelitis; hMOG, human myelin oligodendrocyte glycoprotein; MRI, magnetic resonance imaging. (For interpretation of the references to color in this figure legend, the reader is referred to the web version of this article.)

2.4. Ex vivo MRI acquisition

Ex vivo MRI scans were acquired using Bruker BioSpec® CryoProbe™ for enhanced image quality. The sequences acquired were (a) 3D T1-FLASH with TR = 30 ms, TE = 3.6 ms and a resolution of 0.075 mm × 0.075 mm × 0.1 mm and (b) 3D isotropic T2* with TR = 30 ms, TE = 10 ms and a resolution of 0.1 mm × 0.1 mm × 0.1 mm. DTI was performed by acquiring echo-planar imaging (EPI) with 96 diffusion-weighted directions and a resolution of 0.1095 mm × 0.1099 mm × 0.5 mm. A different T1-weighted sequence was chosen for *ex vivo* scans compared to *in vivo* scans to acquire high resolution *ex-vivo* images using CryoProbe.

2.5. MRI analysis

VGM software (VGMorph GmbH, Mülheim an der Ruhr, Germany) was used for longitudinal analysis of *in vivo* T1-weighted 3D images. In our study, volumes were manually segmented in the axial plane using the pelvic bone and vertebral discs adjacent to vL4 as orientation points. Volume changes relative to the corresponding segmented baseline MRI volume were calculated in VGM on a per voxel basis. Heatmaps were generated from VGM data to illustrate local volume changes. For *ex vivo* T1 scans, five slices were selected from each tissue sample, two being located at opposite ends of the spinal cord segment, and three separating the longitudinal quartiles of the specimen. Since demyelinating lesions were shown to primarily affect the anterolateral white matter tract (ALT) in $hMOG_{1–125}$-induced EAE [31], we chose to focus on this region for the analysis of volume changes. ALT volume changes were assessed as a ratio of the manually segmented ALT area and the entire spinal cord area (ALT/SC ratio) and compared between EAE mice and controls. *Ex vivo* T2* images were analyzed similarly except that we used ITKsnap version 3.8.0 [32] to determine and compare intensity means for the ALT. ALT intensity means of each section were normalized to the adjacent ventral horn gray matter intensity means (ALT/VHGM ratio) to account for MRI gray value variations caused by differences in hardware status and acquisition time. *Ex vivo* DTI scan volumes were aligned using rigid body transformation [33], followed by FA map generation using DSI-Studio [34]. The ALT was manually segmented from five slices per animal and FA values were collected and compared between the two cohorts. T1-weighted *ex vivo* scans were analyzed in VGM by performing a group comparison between EAE mice and controls to assess focal atrophy in specific regions of the spinal cord. VGM determines the local volume differences between two scans by means of a rigid and a non-linear registration. First, each individual EAE mouse was compared to every control mouse, resulting in a set of maps of volume changes for each EAE mouse. These EAE mouse maps were then compared to a common reference to ensure equal spatial orientation. Mean, standard deviation and t-statistics on a per-voxel basis were calculated from the set of registered maps. Multiple-voxel testing was corrected by controlling the false discovery rate at Q = 0.1 using a Benjamini-Hochberg procedure [35] resulting in a threshold of $P = 0.0079$ (corresponding to $-\log_{10}(P = 2.10)$ for statistically significant volume changes).

All scans were viewed, segmented and analyzed based on their intensity means and volumes using the VGM software as well as the open source software applications MRIcron version 1.0.20190902 [36] and ITKsnap version 3.8.0 [32].

2.6. Paraffin embedding

After the completion of *ex vivo* MRI scans, the spinal cord tissue was manually removed from the agarose. Samples were subsequently dehydrated in an ascending series of ethanol before being immersed in xylene and paraffin using the Tissue-Tek VIP 5 Jr. (Umkirch, Germany, Vacuum Infiltration Processor Sakura). For paraffin embedding, the Histocore Arcadia H (Leica, Nussloch, Germany) paraffin embedding station was used. The entire sample was cut into 10 µm-thin transverse sections using a HistoCore Multicut semi-automated microtome (Leica). Three consecutive sections were mounted onto a single Superfrost® (Thermo Scientific, Karlsruhe, Germany) slide. The serial collection of all sections was ensured throughout the entire process to maintain sequential arrangement as in the original sample. Every fifth consecutive slide was used for hematoxylin/eosin (HE) staining or immunohistochemistry, such that slides 1, 6, 11, 16, *etc.* were used for HE staining, while the remaining ones were used for immunohistochemistry (IHC) using different markers.

2.7. HE staining and IHC

HE (Mayer's hemalum, Roth, Karlsruhe, Germany; eosin, Merck, Darmstadt, Germany) staining was performed using a standard protocol [37]. Stained sections were mounted using DPX mountant (Sigma-Aldrich, Taufkirchen, Germany) and coverslipped. IHC was performed as previously described by our group [38]. The following double staining was performed:

(a) Slides 2, 7, 12, 17, *etc.* were stained for myelin basic protein (MBP) and CD3;

(b) Slides 3, 8, 13, 18, *etc.* were stained for glial fibrillary acidic protein (GFAP) and ionized calcium binding adaptor molecule 1 (IBA1);

(c) Slides 4, 9, 14, 19, *etc.* were used for double staining of neurofilament protein H and amyloid precursor protein (APP). Primary antibodies were diluted and incubated in 0.5 % milk powder in tris-buffered saline containing 0.05 % Tween 20 (TBS-T) either overnight at 4 °C or for 3 h at room temperature (RT). All corresponding secondary antibodies were diluted at 1:200 in 0.5 % milk powder in TBS-T and incubated at room temperature for 1 h. All sections were counterstained with Hoechst 33258 (Merck) and mounted using ROTI® Mount Aqua (Roth). Details on all primary and secondary antibodies used in this study are shown in Table 1. Secondary-only control staining served as a negative control on each slide. Tile scans covering each spinal cord section were acquired using a DMi8 Thunder imager (Leica, Wetzlar, Germany) microscope equipped with the HC PL IRAPO (20×/0,75 W) objective and LAS X software (Leica Application Suite X 3.8.2.27713).

2.8. Histological and immunohistochemical analysis

ImageJ software [39] was used for the analysis of all images. Only artifact-free sections were processed. Five HE sections corresponding to the five *ex vivo* T1 MRI scans were selected. ALT white matter and spinal cord total area were manually segmented to calculate the ALT/SC ratio for each of the five selected slices. IHC images were compiled to a hyperstack in ImageJ and the spinal cord total area was manually segmented for each section. Subsequently, upper and lower thresholds were set for the channels to select the stained areas with the following pixel intensity values: GFAP: 1,500-10,000; IBA1: 300–10,000; MBP: 5,500-20,000; CD3: 200–400; SMI-32: 6,000-20,000; APP: 800–1,500.

Table 1
Antibodies used for immunohistochemistry.

Primary antibody	Dilution	Company (# Order number)	Secondary antibody	Company
Anti-CD3 (rabbit monoclonal)	1:200	Abcam (#ab16669)	Cy™3-conjugated donkey anti-rabbit IgG	Jackson ImmunoResearch (#711–165-152)
Anti-IBA1 (rabbit polyclonal)	1:500	FUJIFILM Wako (#019–19,741)		
Anti-APP (rabbit polyclonal)	1:250	Abcam (#ab2072)		
Anti-SMI-32 (mouse monoclonal)	1:500	Calbiochem (#NE-1023)	Cy™2-conjugated donkey anti-mouse IgG	Jackson ImmunoResearch (#715–225-150)
Anti-MBP (mouse monoclonal)	1:800	BioLegend (#808401)		
Anti-GFAP (chicken polyclonal)	1:500	Abcam (#ab4674)	Cy™2-conjugated donkey anti-chicken IgY	Jackson ImmunoResearch (#703–225-155)

APP, amyloid precursor protein; CD3, cluster of differentiation 3; GFAP, glial fibrillary acidic protein; IBA1, ionized calcium binding adaptor molecule 1; MBP, myelin basic protein; SMI-32, anti-neurofilament H non-phosphorylated monoclonal antibody.

The thresholded areas relative to the spinal cord total area were then calculated for every channel in each section.

2.9. Statistical analysis

For each parameter analyzed on MRI scans, or on sections stained either with HE or IHC, a mean value was calculated for every mouse. Each data point in Figs. 3–5 corresponds to this mean value for each respective animal. Statistical analysis was performed using GraphPad Prism (version 9.5.1, Dotmatics., Boston, MA, USA). All group comparisons were perfomed using the Mann-Whitney *U* test. Spearman's correlation coefficient *R* was calculated for the correlation analyses. The level of significance was set at 5 %.

2.10. Data availability

Data not provided in the article because of space limitations may be shared at the request of any qualified investigator for purposes of replicating procedures and results.

3. Results

3.1. Immunization with $hMOG_{1–125}$ induces severe EAE in B6 mice

Clinical EAE scores and weight are shown in Fig. 1B and the main clinical parameters are summarized in Table 2. EAE onset was on day 11.36 ± 0.2 after immunization and the disease reached a peak on day 12.64 ± 0.24 with a mean score of 2.91 ± 0.09, which was accompanied by weight loss. Subsequently, a short period of remission was observed, before mice experienced an EAE relapse, which plateaued around day 45 with a mean clinical score of 2.0 ± 0.12.

3.2. In vivo MRI VGM analysis shows no significant total volume change in the spinal cord of EAE mice

All ($N = 11$) mice developed EAE after immunization, however images of only $N = 6$ animals could be used for *in vivo* analyses due to low quality of the MRI scans of the other $N = 5$ mice. Representative axial slices of *in vivo* T1 MRI scans are shown in Fig. 2A. Heatmaps were derived for each mouse to illustrate longitudinal local volume changes (Fig. 2B). Interestingly, EAE mice and non-immunized controls showed an increase in spinal cord volume over time (Fig. 2C). The calculated volume changes between the final (MRI 5) and the baseline MRI (MRI 0) did not differ between EAE and control mice ($P = 0.47$). Similarly, when comparing volume changes for the final MRI scans relative to the corresponding baseline MRI, there was no statistically significant difference between the two groups ($P = 0.25$).

3.3. EAE mice differ from non-immunized controls in T1- and T2*-weighted ex vivo MRI scans

In *ex vivo* T1-weighted scans, EAE mice displayed a smaller ALT/SC area compared to the controls ($P < 0.001$) as shown in Fig. 3A. Absolute values for the ALT ($P < 0.001$) and the entire spinal cord ($P = 0.013$) were also significantly reduced in EAE mice compared to controls, suggesting a global reduction in volume (Fig. 3A).

Table 2
Clinical EAE parameters.

Parameter	Mean ± Standard Error of the Mean
Day of Onset	11.36 ± 0.20
Mean EAE Score	1.99 ± 0.12
Maximum EAE Score	2.91 ± 0.09
Final EAE Score	2.27 ± 0.14

EAE, experimental autoimmune encephalomyelitis.

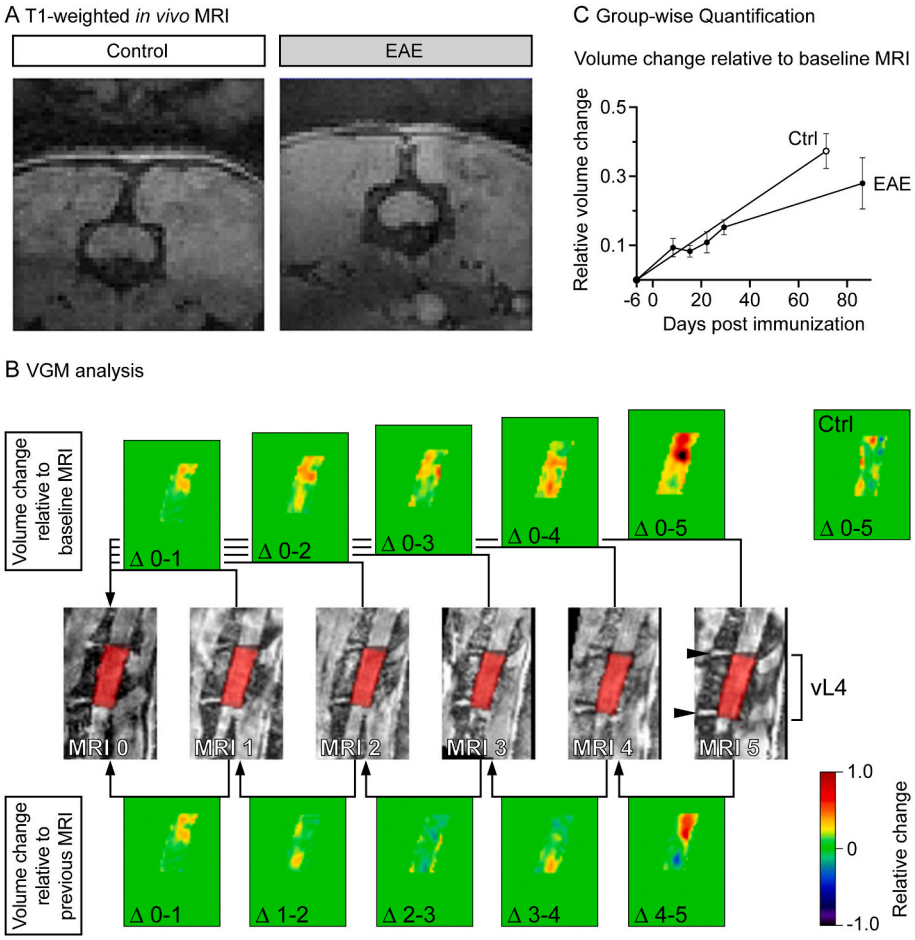

Fig. 2. *In vivo* MRI VGM analysis shows no significant total volume change in the spinal cord of EAE mice.
(A) Representative *in vivo* T1 scan at the level of lumbar vertebral body 4, axial view (TR = 50 ms; TE = 2.5 ms; resolution of 0.13 mm × 0.13 mm × 0.13 mm). (B) Center row shows sagittal views of raw MRI scans of a representative individual EAE mouse. Red overlays indicate manual segmentation of the spinal cord segment vL4, using lumbar body L4 and adjacent vertebral discs as landmarks (indicated by arrowheads in image "MRI 5"). Note that the segmented spinal cord section adjacent to the vertebral body 4 does not correspond to the lumbar spinal cord segment L4. Top row: Heatmaps of local volume changes at each time point relative to the baseline scan. Top right shows local volume changes relative to the baseline scan in a control animal. Bottom row: Heatmaps of local volume changes relative to the preceding scan. (C) Mean volume changes of EAE mice ($N = 6$) and non-immunized controls ($N = 9$) relative to the baseline scans, corresponding to the procedure illustrated in panel B, top row. Ctrl, control; EAE, experimental autoimmune encephalomyelitis; MRI, magnetic resonance imaging; TE, echo time; TR, repetition time; vL4, lumbar spinal cord segment adjacent to vertebra L4; VGM, Voxel-Guided Morphometry. (For interpretation of the references to color in this figure legend, the reader is referred to the web version of this article.)

Fig. 3B displays the resulting VGM heatmaps of regional volume changes of immunized animals compared to controls. The heatmap of volume changes displays the ALT in dark blue, again indicating a local volume reduction of the ALT. The map of statistical significance in Fig. 3B shows color-coded areas with a statistically significant change in volume in red color.

In *ex vivo* T2*-weighted images, the ALT/VHGM intensity ratio was higher in EAE mice compared to controls ($P = 0.02$; Fig. 3A). FA maps were generated from diffusion-weighted MRI images using DSI-Studio. Intensity means were not different between EAE mice and controls ($P = 0.24$).

3.4. Histopathology demonstrates inflammation, demyelination and astrogliosis in the spinal cord of EAE mice

The ALT/SC area ratio was reduced in EAE mice compared to non-immunized controls ($P < 0.001$; Fig. 4), consistent with the *ex vivo* T1 MRI results (Fig. 3A). EAE mice displayed larger GFAP-stained areas compared to controls ($P < 0.001$), likely a sign of active astrogliosis (Fig. 4). Similarly, IBA1-stained areas were larger in EAE mice compared to controls, indicating microglial cells or infiltrating macrophages populating the spinal cord of EAE mice ($P < 0.001$; Fig. 4). Furthermore, reduced MBP-stained areas indicated demyelination in EAE mice compared to controls ($P = 0.002$; Fig. 4). Demyelination was also accompanied by a larger CD3-stained area in the EAE cohort compared to controls ($P = 0.006$) indicating $CD3^+$ T cell infiltration into the spinal cord of the diseased animals. Neurofilament dephosphorylation [40] and APP accumulation [41] are both associated with axonal degeneration. We quantified SMI-32 staining, a marker for non-phosphorylated neurofilament H, and APP staining and did not observe significant differences between $hMOG_{1–125}$-immunized mice and non-immunized controls ($P = 0.82$ for SMI-32 and $P = 0.66$ for APP; Fig. 4).

3.5. MRI outcome parameters correlate with clinical scores and immunohistochemical markers in $hMOG_{1–125}$-induced EAE

The goal of this study was to identify correlations between clinical EAE, MRI, and EAE histopathological parameters, as summarized in the correlation matrix in Fig. 5. Our data show that the reduction of the ALT white matter in EAE mice as determined by T1-weighted *ex vivo* MRI scans correlated with the ALT/SC area in HE-stained sections ($R_S = 0.77$, $P < 0.001$). Clinical EAE scores also correlated with the extent of ALT

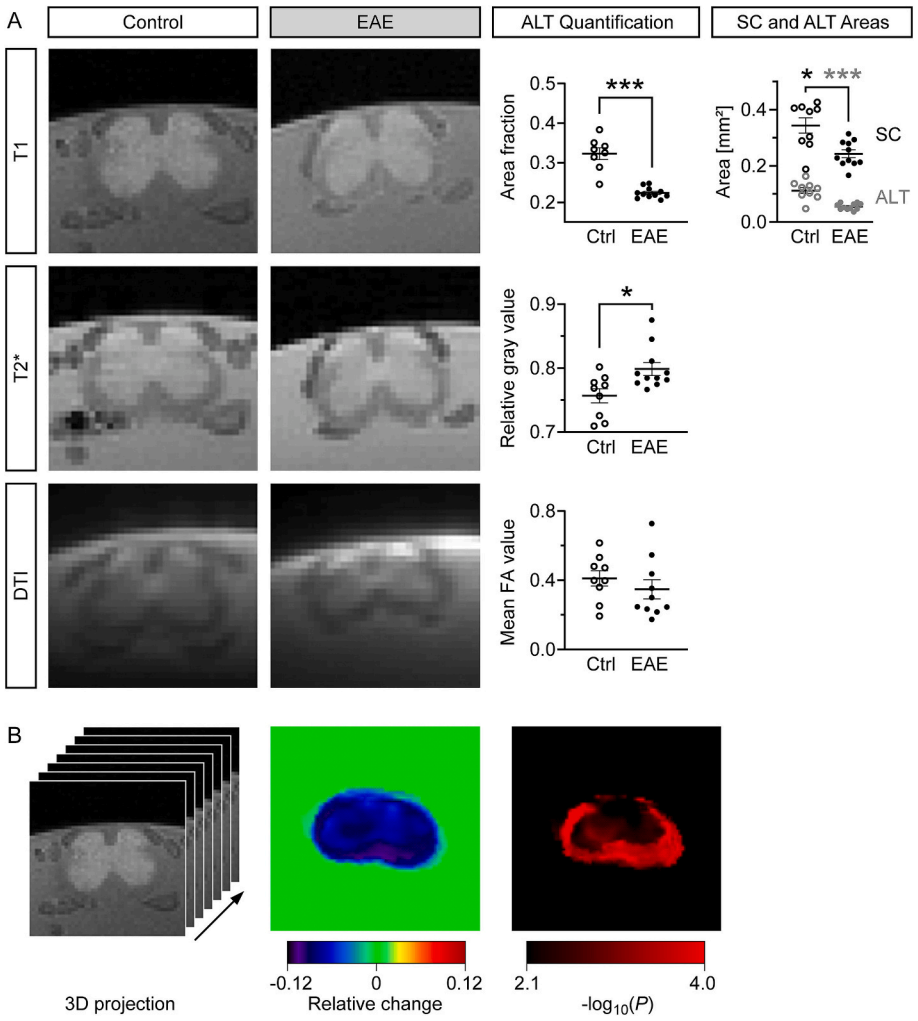

Fig. 3. EAE mice differ from non-immunized controls in T1- and T2*-weighted *ex vivo* MRI scans.
(A) Representative *ex vivo* MRI scans of the lumbar spinal cord, axial view, for EAE mice ($N = 11$) and non-immunized controls ($N = 9$). T1: TR = 30 ms, TE = 3.6 ms; resolution 0.075 mm × 0.075 mm × 0.1 mm; ALT Quantification: area fraction of the ALT relative to the spinal cord cross-sectional area; SC and ALT areas: absolute SC (black dots) and ALT areas in mm^2 (gray dots). T2*: TR = 30 ms, TE = 10 ms, resolution 0.1 mm × 0.1 mm × 0.1 mm, quantified as intensity mean of the ALT relative to the intensity mean of adjacent gray matter. DTI: echo-planar imaging (EPI) with 96 diffusion-weighted directions, resolution 0.1095 mm × 0.1099 mm × 0.5 mm, quantified as mean FA value of ALT. * $P < 0.05$; *** $P \leq 0.005$. (B) VGM analysis of *ex vivo* T1 scans as a group comparison between EAE mice ($N = 11$) and non-immunized controls ($N = 9$). Left: Illustration of stacked axial MRI slices for 3D sample reconstruction. Local relative volume changes were axially projected for comparison between EAE mice and controls in VGM group analysis. Axially projected group differences are presented as heatmaps of relative local changes (middle), and local statistical significance (right). Significantly different areas are indicated by red color, with a cut-off for statistical significance at $P < 0.0079$ (or $-\log_{10}(P) > 2.10$). ALT, anterolateral tract; Ctrl, control; EAE, experimental autoimmune encephalomyelitis; DTI, diffusion tensor imaging; EPI, echo-planar imaging; FA, functional anisotropy; MRI, magnetic resonance imaging; SC, spinal cord; TR, repetition time; TE, echo time; VGM, Voxel-Guided Morphometry. (For interpretation of the references to color in this figure legend, the reader is referred to the web version of this article.)

white matter loss, as determined either by T1-weighted *ex vivo* MRI ($R_S = -0.84$; $P < 0.001$) or HE staining ($R_S = -0.75$; $P < 0.001$). Thus, clinically relevant differences in ALT white matter reduction could be measured by *ex vivo* T1-weighted MRI in EAE-induced mice.

Statistically significant inverse correlations were observed between most histopathological markers and the *ex vivo* T1-weighted MRI-based ALT/SC area (GFAP: $R_S = -0.74$, $P < 0.001$; IBA1: $R_S = -0.69$, $P < 0.001$; CD3: $R_S = -0.69$, $P < 0.001$). Clinical EAE scores positively correlated with the histopathological markers GFAP ($R_S = 0.87$, $P < 0.001$), IBA1 ($R_S = 0.84$, $P < 0.001$) and CD3 ($R_S = 0.66$, $P = 0.001$), and showed an inverse correlation with MBP ($R_S = -0.63$, $P = 0.003$).

T2*-weighted ALT intensities inversely correlated with the ALT/SC area measured either on *ex vivo* T1 scans ($R_S = -0.58$, $P = 0.007$), or in HE-stained sections ($R_S = -0.6$, $P = 0.005$), showing that a reduced ALT area is associated with higher intensity means in T2*-weighted MRI. Furthermore, increased intensity means on T2*-weighted MRI scans positively correlated with higher EAE scores ($R_S = 0.6$, $P = 0.005$) and histopathological markers (GFAP: $R_S = 0.53$, $P = 0.016$; CD3: $R_S = 0.51$, $P = 0.02$). This suggests that increased T2*-weighted ALT intensity means are associated with ALT white matter loss and higher clinical EAE scores.

Finally, histopathological parameters were mutually correlated, with the strongest correlation between GFAP and IBA1 ($R_S = 0.88$, $P < 0.001$). Only MBP correlated inversely with the other histopathological markers.

4. Discussion

Using MRI as a read-out parameter, we set out to investigate whether longitudinally measured volume changes in the spinal cord of EAE mice were associated with clinical disease severity and well-established histopathological markers, where an increase or decrease in volume could

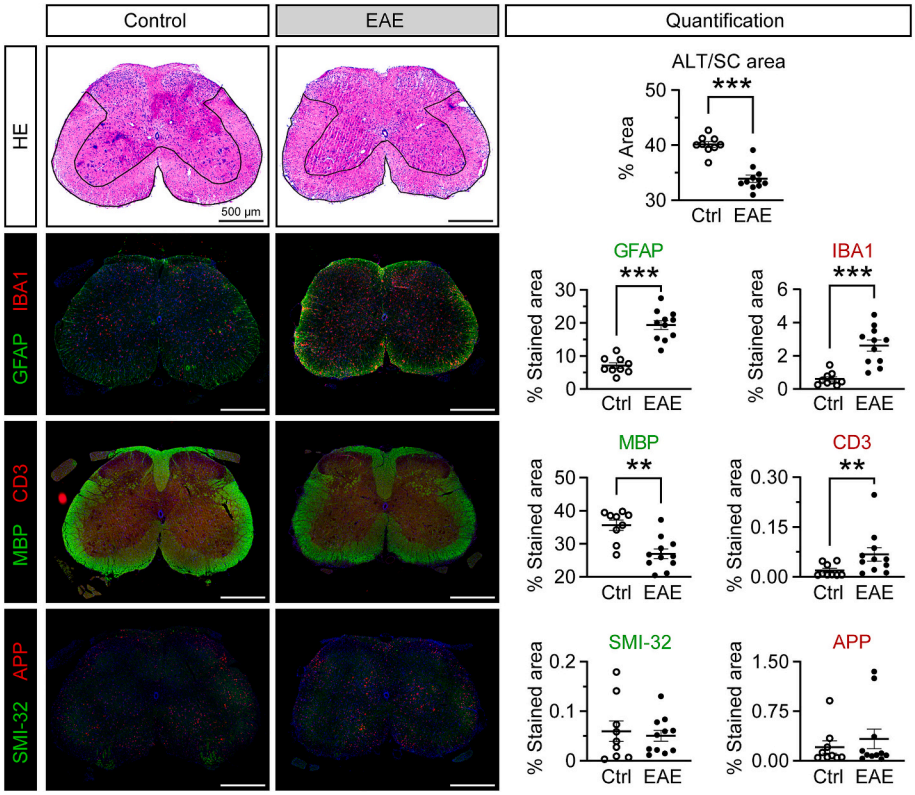

Fig. 4. Histopathology demonstrates inflammation, demyelination and astrogliosis in the spinal cord of EAE mice.
Analysis of histopathological parameters in EAE mice ($N = 11$) compared to non-immunized controls ($N = 9$), showing representative 10 µm-thin spinal cord cross sections. HE: The black outline illustrates the manually segmented ALT which was quantified as ALT area relative to the area of entire spinal cord section (ALT/SC area). Immunohistochemistry: Representative images show GFAP/IBA1, MBP/CD3 and SMI-32/APP double staining, quantified as thresholded stained area relative to the area of entire spinal cord. ** $P \leq 0.01$; *** $P \leq 0.005$. ALT, anterolateral tract; APP, amyloid precursor protein; CD3, cluster of differentiation 3; Ctrl, control; EAE, experimental autoimmune encephalomyelitis; GFAP, glial fibrillary acidic protein; HE, hematoxylin eosin; IBA1, ionized calcium binding adaptor molecule 1; MBP, myelin basic protein; SC, spinal cord; SMI-32, anti-neurofilament H non-phosphorylated monoclonal antibody.

indicate inflammation or tissue atrophy, respectively. We used VGM as a method which allows tracking of regional volume changes over the whole tissue on a voxel-by-voxel basis between multiple time points [14].

The data presented here demonstrate a steady increase in the overall spinal cord volume irrespective of the group (EAE mice *vs.* controls), possibly due to body growth and/or spinal cord maturation over the course of our longitudinal study as indicated by the increase in body weight (Fig. 1B). Yet, the change in body sizes may have also introduced a segmentation bias for the spinal cord volume, as the analyzed spinal cord segment was defined relative to the adjacent vL4. Unlike *ex vivo* T1 MRI scans, segmentation of *in vivo* MRI scans showed no differences in the relative volume changes of the spinal cord between the EAE cohort and the controls (Fig. 2C). Nevertheless, the strength of using VGM lies in its ability to identify anatomically localized volume changes in tissues of interest over the course of a longitudinal study [14]. We hypothesized that VGM could detect localized tissue expansion in the EAE cohort, as a possible result of edema and immune cell infiltration. However, given the limited resolution of *in vivo* T1 scans (0.13 mm × 0.13 mm × 0.13 mm), visual identification of inflammatory lesions was not feasible, even with VGM.

Atrophy as a pathological parameter has been investigated in patients [42] as well as in the animal model of MS, where studies have revealed that there is a reduction in volume of white matter tracts such as in the corpus callosum in $MOG_{35–55}$-induced EAE [43]. Our results confirm these observations made by other groups in that they indicate a global reduction in volume of the lumbar spinal cord. A more detailed analysis of the ALT/SC ratio on *ex vivo* T1 MRI scans revealed a significant reduction of the anterolateral white matter in EAE mice compared to controls, which was consistent with the reduction of the ALT/SC ratio as measured in HE-stained sections (Figs. 3–5). These data underline the suitability of T1-weighted MRI scans to represent anatomical correlates of pathology [44].

Furthermore, the ALT white matter of EAE mice showed significantly increased intensities on T2*-weighted *ex vivo* MRI scans compared to controls (Fig. 3A). T2*-weighted MRI can be used to quantify iron deposition in a given organ [45], where iron deposits present as hypointense dots or rings [17]. However, our *ex vivo* MRI scans showed no detectable MRI hypointensities in the $hMOG_{1–125}$-immunized cohort, but instead T2* hyperintensity. This unexpected finding possibly results from demyelination and axonal loss [46]. Indeed, higher T2* intensity means were associated with larger SMI-32-stained areas in sections of the lumbar spinal cord ($R_S = 0.75$, $P < 0.001$).

No statistically significant differences were observed for APP and SMI-32 when comparing EAE mice and controls. Previous studies in MS patients have shown that both markers can mainly be detected in acute CNS lesions and that their presence decreases with further progress of the disease [47,48]. This could explain why we hardly observed APP- and/or SMI-32-positive axons in our mice.

Our data also indicate that higher EAE clinical scores were related to smaller ALT/SC areas on *ex vivo* T1 scans and in HE-stained sections. Furthermore, the final score was associated with most of the histopathological parameters that were tested, notably GFAP, IBA1, MBP and CD3, indicating astrogliosis, microglial activation/macrophage infiltration, demyelination and T cell infiltration, respectively. Thus, the severity of EAE was reflected not only in the *ex vivo* T1 and T2* scans but also in the overall histopathology.

Taken together, our study demonstrates that MRI measurements of

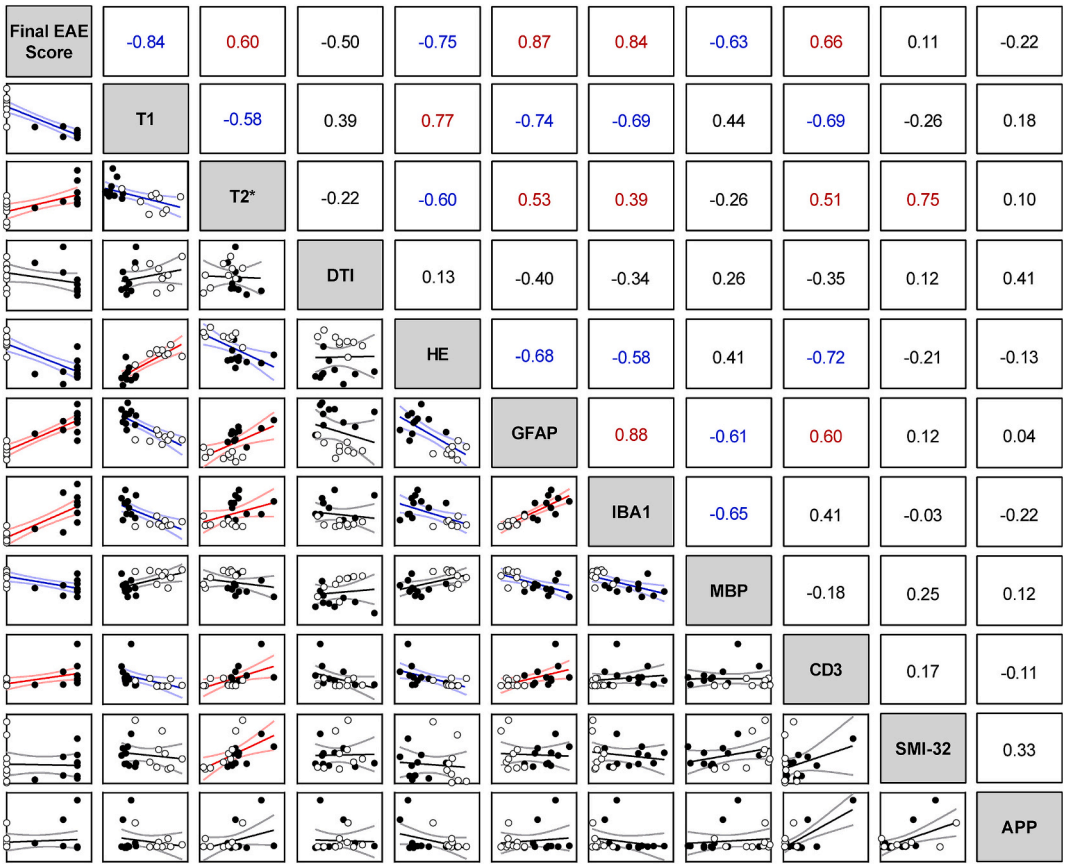

Fig. 5. MRI outcome parameters correlate with the final EAE score and immunohistochemical markers in $hMOG_{1–125}$-induced EAE.
Correlation matrix of the final EAE score, MRI parameters and immunohistochemical markers. The diagonal shows parameters of pairwise correlation. In scatter plots below the diagonal, each x-axis represents the parameter in the corresponding column of the scatter plot, while each y-axis represents the parameter in the corresponding row of the scatter plot. Regression lines (black, blue or red lines) and 95 % confidence intervals (gray, light blue, or light red lines) are illustrated in the scatter plots. Control values are presented as white and EAE values as black circles. Spearman's correlation coefficients are shown above the diagonal. Significant R_S values ($P < 0.05$) are marked with red color for positive correlation and blue for inverse correlation. Parameters "T1" and "HE" both indicate the area of anterolateral tract relative to the total spinal cord section area (ALT/SC area). APP, amyloid precursor protein; CD3, cluster of differentiation 3; DTI, diffusion tensor imaging; EAE, experimental autoimmune encephalomyelitis; GFAP, glial fibrillary acidic protein; HE, hematoxylin eosin; $hMOG_{1–125}$, human myelin oligodendrocyte glycoprotein 1–125; IBA1, ionized calcium binding adaptor molecule 1; MBP, myelin basic protein; MRI, magnetic resonance imaging; SMI-32, anti-neurofilament H non-phosphorylated monoclonal antibody. (For interpretation of the references to color in this figure legend, the reader is referred to the web version of this article.)

anatomical changes in the spinal cord can be correlated with clinical disease and histopathological parameters in an animal model of MS. Moreover, we show that volume changes caused by EAE-induced pathology can be monitored by VGM. In our study, sub-millimeter histological changes in the spinal cord of EAE mice were detectable on *ex vivo* MRI scans of isolated spinal cord specimens. However, due to limitations of MRI scan time and resolution, *in vivo* MRI scans showed only a trend towards a lumbar spinal cord volume reduction in EAE mice compared to controls, without reaching statistical significance (Fig. 2). Improving the spatial resolution of MRI scans, for example by decreasing voxel sizes within a specified region of interest or increasing the scan time, would not only allow to monitor lesion development and progression over time in EAE, but also pave the way for successful CNS lesion classification, which is currently only possible by *post mortem* histological analysis.

Funding

This study was supported by the BONFOR research funding program of the Faculty of Medicine of the University of Bonn (project 2022-4-23, grant to S.K.) and by the German Research Foundation (Deutsche Forschungsgemeinschaft, DFG) project 460333672 CRC1540 EBM (project B04, principial investigator S.K.).

Author contribution

A.L., A.D., M.K., and S.K. conceived and designed the study. A.L., H. D., M.H., R.C., A.W. and S.K. performed the experiments. A.L., A.D. and R.C. were responsible for statistical analysis. A.L., M.H., R.C. and S.K. drafted the manuscript. All authors contributed to the article and approved the submitted version.

CRediT authorship contribution statement

Anna Lowinski: Writing – original draft, Visualization, Methodology, Formal analysis, Data curation, Conceptualization. **Andreas Dabringhaus:** Writing – review & editing, Supervision, Software, Formal analysis, Conceptualization. **Matthias Kraemer:** Writing – review & editing, Conceptualization. **Hardik Doshi:** Writing – review & editing, Supervision, Software, Methodology, Investigation, Conceptualization. **Alicia Weier:** Writing – review & editing, Visualization, Methodology. **Maik Hintze:** Writing – review & editing, Visualization, Formal analysis. **Rittika Chunder:** Writing – original draft. **Stefanie Kuerten:** Writing – original draft, Validation, Supervision, Resources, Project administration, Methodology, Investigation, Funding acquisition, Data curation, Conceptualization.

Declaration of competing interest

A.L., H.D., A.W., M.H. have nothing to declare. A.D. and M.K. are the founders of VGMorph GmbH. R.C. received funding from the DFG under Germany's Excellence Strategy – EXC2151–390873048 and from Novartis (Oppenheim-Förderpreis für Multiple Sklerose 2023). S.K. reports funding from Novartis, F. Hoffmann-La Roche and Sanofi; and speaker fees and consultancy honoraria from Novartis, F. Hoffmann-La Roche, Sanofi, and Teva. S.K. is also supported by the DFG IRTG 2168, grant no. 272482170, the DFG project 460,333,672 CRC1540 EBM, and she is a member of the Excellence Cluster "ImmunoSensation^{2}" EXC2151–390873048.

Acknowledgement

The authors would like to thank Doris Bittner, Birgit Blanck, Marion Michels and Ji-Young Chang for excellent technical and administrative assistance.

References

[1] R. Dobson, G. Giovannoni, Multiple sclerosis – a review, Eur. J. Neurol. 26 (1) (2019) 27–40, https://doi.org/10.1111/ene.13819.
[2] B. Engelhardt, M. Comabella, A. Chan, Multiple sclerosis: immunopathological heterogeneity and its implications, Eur. J. Immunol. 52 (6) (2022) 869–881, https://doi.org/10.1002/eji.202149757.
[3] C. Baecher-Allan, B.J. Kaskow, H.L. Weiner, Multiple sclerosis: mechanisms and immunotherapy, Neuron 97 (4) (2018) 742–768, https://doi.org/10.1016/j.neuron.2018.01.021.
[4] B.A.C. Cree, D.L. Arnold, J. Chataway, et al., Secondary progressive multiple sclerosis: new insights, Neurology 97 (8) (2021) 378–388, https://doi.org/10.1212/WNL.0000000000012323.
[5] D.H. Miller, S.M. Leary, Primary-progressive multiple sclerosis, Lancet Neurol. 6 (10) (2007) 903–912, https://doi.org/10.1016/S1474-4422(07)70243-0.
[6] H. Lassmann, Multiple sclerosis pathology, Cold Spring Harb. Perspect. Med. 8 (3) (2018) a028936, https://doi.org/10.1101/cshperspect.a028936.
[7] H. Lassmann, J. Van Horssen, D. Mahad, Progressive multiple sclerosis: pathology and pathogenesis, Nat. Rev. Neurol. 8 (11) (2012) 647–656, https://doi.org/10.1038/nrneurol.2012.168.
[8] K.E. Attfield, L.T. Jensen, M. Kaufmann, M.A. Friese, L. Fugger, The immunology of multiple sclerosis, Nat. Rev. Immunol. 22 (12) (2022) 734–750, https://doi.org/10.1038/s41577-022-00718-z.
[9] G. Disanto, A.J. Berlanga, A.E. Handel, et al., Heterogeneity in multiple sclerosis: scratching the surface of a complex disease, Autoimmune Dis. 2011 (2011) 1–12, https://doi.org/10.4061/2011/932351.
[10] M.P. McGinley, C.H. Goldschmidt, A.D. Rae-Grant, Diagnosis and treatment of multiple sclerosis: a review, JAMA 325 (8) (2021) 765, https://doi.org/10.1001/jama.2020.26858.
[11] A.J. Thompson, B.L. Banwell, F. Barkhof, et al., Diagnosis of multiple sclerosis: 2017 revisions of the McDonald criteria, Lancet Neurol. 17 (2) (2018) 162–173, https://doi.org/10.1016/S1474-4422(17)30470-2.
[12] M.P. Wattjes, O. Ciccarelli, D.S. Reich, et al., 2021 MAGNIMS–CMSC–NAIMS consensus recommendations on the use of MRI in patients with multiple sclerosis, Lancet Neurol. 20 (8) (2021) 653–670, https://doi.org/10.1016/S1474-4422(21)00095-8.
[13] M. Filippi, M.A. Rocca, O. Ciccarelli, et al., MRI criteria for the diagnosis of multiple sclerosis: MAGNIMS consensus guidelines, Lancet Neurol. 15 (3) (2016) 292–303, https://doi.org/10.1016/S1474-4422(15)00393-2.
[14] A. Raj, A. Gass, P. Eisele, A. Dabringhaus, M. Kraemer, F.G. Zöllner, A generalizable deep voxel-guided morphometry algorithm for the detection of subtle lesion dynamics in multiple sclerosis, Front. Neurosci. 18 (2024) 1326108, https://doi.org/10.3389/fnins.2024.1326108.
[15] J. Fox, M. Kraemer, T. Schormann, et al., Individual assessment of brain tissue changes in MS and the effect of focal lesions on short-term focal atrophy development in MS: a voxel-guided morphometry study, Int. J. Mol. Sci. 17 (4) (2016) 489, https://doi.org/10.3390/ijms17040489.
[16] E. Sbardella, F. Tona, N. Petsas, P. Pantano, DTI measurements in multiple sclerosis: evaluation of brain damage and clinical implications, Mult. Scler. Int. 2013 (2013) 1–11, https://doi.org/10.1155/2013/671730.
[17] G.B. Chavhan, P.S. Babyn, B. Thomas, M.M. Shroff, E.M. Haacke, Principles, techniques, and applications of T2*-based MR imaging and its special applications, Radiographics 29 (5) (2009) 1433–1449, https://doi.org/10.1148/rg.295095034.
[18] J.M. Stankiewicz, M. Neema, A. Ceccarelli, Iron and multiple sclerosis, Neurobiol. Aging 35 (2014) S51–S58, https://doi.org/10.1016/j.neurobiolaging.2014.03.039.
[19] J.A. Reeves, M. Mohebbi, T. Wicks, et al., Paramagnetic rim lesions predict greater long-term relapse rates and clinical progression over 10 years, Mult. Scler. 30 (4–5) (2024) 535–545, https://doi.org/10.1177/13524585241229956.
[20] C.E. Weber, M. Wittayer, M. Kraemer, et al., Long-term dynamics of multiple sclerosis iron rim lesions, Mult. Scler. Relat. Disord. 57 (2022) 103340, https://doi.org/10.1016/j.msard.2021.103340.
[21] N.W. Schurink, S.R. Van Kranen, S. Roberti, et al., Sources of variation in multicenter rectal MRI data and their effect on radiomics feature reproducibility, Eur. Radiol. 32 (3) (2022) 1506–1516, https://doi.org/10.1007/s00330-021-08251-8.
[22] A.J. Solomon, R.T. Naismith, A.H. Cross, Misdiagnosis of multiple sclerosis: impact of the 2017 McDonald criteria on clinical practice, Neurology 92 (1) (2019) 26–33, https://doi.org/10.1212/WNL.0000000000006583.
[23] M. Filippi, P. Preziosa, F. Barkhof, et al., Diagnosis of progressive multiple sclerosis from the imaging perspective: a review, JAMA Neurol. 78 (3) (2021) 351, https://doi.org/10.1001/jamaneurol.2020.4689.
[24] T. Kuhlmann, H. Lassmann, W. Brück, Diagnosis of inflammatory demyelination in biopsy specimens: a practical approach, Acta Neuropathol. 115 (3) (2008) 275–287, https://doi.org/10.1007/s00401-007-0320-8.
[25] M.Y. Khodanovich, T.V. Anan'ina, E.P. Krutenkova, et al., Challenges and practical solutions to MRI and histology matching and measurements using available ImageJ software tools, Biomedicines 10(7):1556 (2022), https://doi.org/10.3390/biomedicines10071556.
[26] C.A. Humphreys, M.A. Jansen, S. Muñoz Maniega, et al., A protocol for precise comparisons of small vessel disease lesions between ex vivo magnetic resonance imaging and histopathology, Int. J. Stroke 14 (3) (2019) 310–320, https://doi.org/10.1177/1747493018799962.
[27] H. Kolb, O. Al-Louzi, E.S. Beck, P. Sati, M. Absinta, D.S. Reich, From pathology to MRI and back: clinically relevant biomarkers of multiple sclerosis lesions, NeuroImage Clin. 36 (2022) 103194, https://doi.org/10.1016/j.nicl.2022.103194.
[28] S. Bittner, A.M. Afzali, H. Wiendl, S.G. Meuth, Myelin oligodendrocyte glycoprotein (MOG_{35-55}) induced experimental autoimmune encephalomyelitis (EAE) in C57BL/6 mice, JoVE 86 (2014) 51275, https://doi.org/10.3791/51275.
[29] C. Kilkenny, W.J. Browne, I.C. Cuthill, M. Emerson, D.G. Altman, Improving bioscience research reporting: the ARRIVE guidelines for reporting animal research, PLoS 29;8(6):e1000412 (2010), https://doi.org/10.1371/journal.pbio.1000412.
[30] M. Harrison, A. O'Brien, L. Adams, et al., Vertebral landmarks for the identification of spinal cord segments in the mouse, Neuroimage 68 (2013) 22–29, https://doi.org/10.1016/j.neuroimage.2012.11.048.
[31] T. Breakell, S. Tacke, V. Schropp, et al., Obinutuzumab-induced B cell depletion reduces spinal cord pathology in a CD20 double transgenic mouse model of multiple sclerosis, IJMS 21 (18) (2020) 6864, https://doi.org/10.3390/ijms21186864.
[32] ITK-SNAP Home. Accessed May 20, 2024, http://www.itksnap.org/pmwiki/pmwiki.php.
[33] Z. Zhou, W. Liu, J. Cui, et al., Automated artifact detection and removal for improved tensor estimation in motion-corrupted DTI data sets using the combination of local binary patterns and 2D partial least squares, Magn. Reson. Imaging 29 (2) (2011) 230–242, https://doi.org/10.1016/j.mri.2010.06.022.
[34] DSI Studio Documentation. DSI Studio Documentation. Accessed May 20, 2024, https://dsi-studio.labsolver.org/download.html.
[35] C.R. Genovese, N.A. Lazar, T. Nichols, Thresholding of statistical maps in functional neuroimaging using the false discovery rate, Neuroimage 15 (4) (2002) 870–878, https://doi.org/10.1006/nimg.2001.1037.
[36] NITRC: MRIcron: Tool/Resource Info. Accessed May 20, 2024, https://www.nitrc.org/projects/mricron/.
[37] A.H. Fischer, K.A. Jacobson, J. Rose, R. Zeller, Hematoxylin and eosin staining of tissue and cell sections, CSH Protoc. 2008(5):pdb.prot4986 (2008), https://doi.org/10.1101/pdb.prot4986.
[38] A. Weier, M. Enders, P. Kirchner, et al., Impact of siponimod on enteric and central nervous system pathology in late-stage experimental autoimmune encephalomyelitis, Int. J. Mol. Sci. 23 (22) (2022) 14209, https://doi.org/10.3390/ijms232214209.
[39] Fiji. ImageJ Wiki. Accessed May 20, 2024, https://imagej.github.io/software/fiji/index.
[40] B.D. Trapp, J. Peterson, R.M. Ransohoff, R. Rudick, S. Mörk, L. Bö, Axonal transection in the lesions of multiple sclerosis, N. Engl. J. Med. 338 (5) (1998) 278–285, https://doi.org/10.1056/NEJM199801293380502.
[41] M.J. Craner, J. Newcombe, J.A. Black, C. Hartle, M.L. Cuzner, S.G. Waxman, Molecular changes in neurons in multiple sclerosis: altered axonal expression of $Na_v1.2$ and $Na_v1.6$ sodium channels and Na^+/ca^{2+} exchanger, Proc. Natl. Acad. Sci. USA 101 (21) (2004) 8168–8173, https://doi.org/10.1073/pnas.0402765101.
[42] A. Andravizou, E. Dardiotis, A. Artemiadis, et al., Brain atrophy in multiple sclerosis: mechanisms, clinical relevance and treatment options, Auto Immun Highlights. 10 (1) (2019) 7, https://doi.org/10.1186/s13317-019-0117-5.
[43] A.M. Hamilton, N.D. Forkert, R. Yang, et al., Central nervous system targeted autoimmunity causes regional atrophy: a 9.4T MRI study of the EAE mouse model of multiple sclerosis, Sci. Rep. 9(1):8488 (2019), https://doi.org/10.1038/s41598-019-44682-6.
[44] R. Bitar, G. Leung, R. Perng, et al., MR pulse sequences: what every radiologist wants to know but is afraid to ask, Radiographics 26 (2) (2006) 513–537, https://doi.org/10.1148/rg.262055063.
[45] P.A. Wahidiyat, S.D. Iskandar, D. Sekarsari, Evaluation of iron overload between age groups using magnetic resonance imaging and its correlation with iron, Acta Med. Indones. 50 (3) (2018) 230–236.

[46] S. Debette, H.S. Markus, The clinical importance of white matter hyperintensities on brain magnetic resonance imaging: systematic review and meta-analysis, BMJ 341(jul26 1):c3666-c3666 (2010), https://doi.org/10.1136/bmj.c3666.
[47] J. Gehrmann, R.B. Banati, M.L. Cuzner, G.W. Kreutzberg, J. Newcombe, Amyloid precursor protein (APP) expression in multiple sclerosis lesions, Glia 15 (2) (1995) 141–151, https://doi.org/10.1002/glia.440150206.
[48] L. Schirmer, J.P. Antel, W. Brück, C. Stadelmann, Axonal loss and neurofilament phosphorylation changes accompany lesion development and clinical progression in multiple sclerosis, Brain Pathol. 21 (4) (2011) 428–440, https://doi.org/10.1111/j.1750-3639.2010.00466.x.